Author Manuscript

Author Manuscript

Author Manuscript

Author Manuscript

HHS Public Access

Author manuscript

Brain Behav Immun. Author manuscript; available in PMC 2022 May 19.

Published in final edited form as:

Brain Behav Immun. 2021 November ; 98: 122–135. doi:10.1016/j.bbi.2021.08.210.

Novel microglia-mediated mechanisms underlying synaptic loss and cognitive impairment after traumatic brain injury

Karen Krukowski[a,b,1], **Amber Nolan**[a,b,1], **McKenna Becker**[a,b], **Katherine Picard**[g], **Nathalie Vernoux**[g], **Elma S. Frias**[a,b,c], **Xi Feng**[a,b], **Marie-Eve Tremblay**[g,h,i,j,*], **Susanna Rosi**[a,b,c,d,e,f,*]

[a] Department of Physical Therapy and Rehabilitation Science, University of California, San Francisco, CA, USA

[b] Brain and Spinal Injury Center, University of California, San Francisco, CA, USA

[c] Department of Biomedical Sciences, University of California, San Francisco, CA, USA

[d] Department of Neurological Surgery, University of California, San Francisco, CA, USA

[e] Weill Institute for Neuroscience, University of California San Francisco, CA, USA

[f] Kavli Institute of Fundamental Neuroscience, University of California San Francisco, CA, USA

[g] Axe Neurosciences, CRCHU de Québec-Université Laval, Québec, QC, Canada

[h] Molecular Medicine Department, Université Laval, Québec, QC, Canada

[i] Division of Medical Sciences, University of Victoria, Victoria, BC, Canada

[j] Department of Biochemistry and Molecular Biology, The University of British Columbia, Vancouver, BC, Canada

Abstract

Traumatic brain injury (TBI) is one of the leading causes of long-term neurological disability in the world. Currently, there are no therapeutics for treating the deleterious consequences of brain trauma; this is in part due to a lack of complete understanding of cellular processes that underlie TBI-related pathologies. Following TBI, microglia, the brain resident immune cells, turn into a "reactive" state characterized by the production of inflammatory mediators that contribute to the development of cognitive deficits. Utilizing multimodal, state-of-the-art techniques that widely span from ultrastructural analysis to optogenetic interrogation of circuit function, we investigated the reactive microglia phenotype one week after injury when learning and memory deficits are also measured. Microglia displayed increased: (i) phagocytic activity *in vivo*, (ii) synaptic

This is an open access article under the CC BY-NC-ND license (http://creativecommons.org/licenses/by-nc-nd/4.0/).

* Corresponding authors at: Medical Sciences Building, Room 322, University of Victoria, Victoria, BC V8W 2Y2, Canada (M.-E. Tremblay). 1001 Potrero Ave, Zuckerberg San Francisco General Hospital, Building#1 room 101, San Francisco, CA 94110 (S. Rosi). evetremblay@uvic.ca (M.-E. Tremblay), susanna.rosi@ucsf.edu (S. Rosi).

[1]Authors contributed equally.

Declaration of Competing Interest

The authors declare that they have no known competing financial interests or personal relationships that could have appeared to influence the work reported in this paper.

Appendix A. Supplementary data

Supplementary data to this article can be found online at https://doi.org/10.1016/j.bbi.2021.08.210.

Author Manuscript Author Manuscript Author Manuscript Author Manuscript

engulfment, (iii) increased neuronal contact, including with dendrites and somata (termed ‘satellite microglia’). Functionally, satellite microglia might impact somatic inhibition as demonstrated by the associated reduction in inhibitory synaptic drive. Cumulatively, here we demonstrate novel microglia-mediated mechanisms that may contribute to synaptic loss and cognitive impairment after traumatic brain injury.

Keywords

Traumatic brain injury; Microglia; Neuroinflammation; Learning and memory

1. Introduction

Microglia are highly motile cells that make up the innate immunity of the central nervous system (CNS). In physiological conditions, microglia respond to pathogen detection and tissue repair but also sculpt neuronal circuits and influence neuronal activity (Tremblay et al., 2010; Li et al., 2012; Schafer et al., 2012; Parkhurst et al., 2013; Badimon et al., 2020). Much of this influence on neuronal activity is through microglial interaction with synapses. Microglia are considered the fourth component of the ‘quad-partite synapse’, the other three being presynaptic axon terminals, postsynaptic dendritic spines, and perisynaptic astrocytic processes (Bennett, 2007; Tremblay and Majewska, 2011; Schafer et al., 2013). This component contributes to the formation and maturation of spines and the elimination of synapses through engulfment (also termed “synaptic pruning”). Elimination of synapses has been shown to be mediated by the classical complement and triggering receptor expressed on myeloid cells 2 (TREM2) pathways, as well as fractalkine signaling between neuronal chemokine CX_3CL1 and its unique receptor, CX_3CR1, expressed by microglia (Schafer et al., 2012; Paolicelli et al., 2011; Gunner et al., 2019). The pruning process involves phagocytosis and one of its specialized forms, named “trogocytosis” (nibbling), of synaptic structures (Weinhard et al., 2018). Phagocytosis of synaptic structures is not the only interaction of microglia with synapses. A lesser-known interaction of microglia with synapses is their ability to insert their processes and/or wrap around the neuronal membrane separating pre- and post-synaptic structures in a process termed ‘synaptic stripping’ (Blinzinger and Kreutzberg, 1968; Trapp et al., 2007). Surveillant microglia interact with synapses in the mature, healthy brain, directly leading to an increase in synaptic activity that synchronizes local populations of neurons. The increased synaptic activity and consequent neuronal synchrony associated with microglial interaction is lost after systemic lipopolysaccharide (LPS) administration (Akiyoshi, et al., 2018). LPS is the most commonly known proinflammatory stimulus for microglia reactivity. These data suggest that microglial reactivity might directly affect neuronal circuit function.

Microglial reactivity is a prominent feature of traumatic brain injury (TBI), and microgliosis can persist for years following the initial injury (Nagamoto-Combs et al., 2007; Ramlackhansingh et al., 2011; Johnson et al., 2013). While acutely microglia contribute to restoring homeostasis after the injury, persistently reactive microglia produce proinflammatory/cytotoxic molecules contributing to neuronal damage (Morganti et al., 2015; Loane and Kumar, 2016; Donat et al., 2017). Indeed, depletion of microglia has been

Author Manuscript Author Manuscript Author Manuscript Author Manuscript

shown to ameliorate the neurological outcome of TBI in rodents (reviewed in (Paladini et al., 2021). However, the specific mechanisms by which microglia impact synaptic interactions that directly shape circuit function, especially in the context of TBI, are yet unknown.

To address these questions, we used our well-established translational mouse model of TBI and employed a combination of state-of-the-art techniques: 1) ultrastructural analyses by immunocytochemical transmission electron microscopy, 2) *in vivo* phagocytosis assay, 3) synaptosome quantification, 4) confocal microscopy and 5) optogenetic evaluation of circuit function to provide insights to the microglia-mediated mechanisms underlying synaptic loss and behavioral impairment in TBI.

2. Results

2.1. Spacial learning and memory deficits following traumatic brain Injury.

We have previously reported the chronic consequences of unilateral, focal contusion injury (Xiong et al., 2013) on learning and memory functions (Morganti et al., 2015; Chou et al., 2017; Chou et al., 2018; Krukowski et al., 2018); here, we aimed to investigate cognitive phenotypes shortly after injury. We measured spatial learning and memory in male and female adult mice using the radial arm water maze as previously described (Alamed et al., 2006). In this forced-swim test, mice were trained (Fig. 1A – L'earning') on Day 7 post injury (three blocks of 3 trials each) to locate a platform hidden under the opaque water in one of the eight arms using navigational cues in the room (Fig. 1A). Spatial memory was tested by running a single block probe twenty-four hours later (Day 8 – 'Memory Probe', Fig. 1A). The total number of entries into arms that did not contain the platform (termed errors) before locating the escape platform were used as a metric of spatial learning and memory, a deficit frequently reported in patients that suffered TBI from a range of mild to severe injury (McAllister et al., 2001; Palacios et al., 2012; Manktelow et al., 2017).

Similar to human TBI, impairments in spatial learning were measured in mice seven days after injury (dpi) compared with sham (uninjured) animals (Fig. 1B). Furthermore, the TBI-induced learning deficits were paralleled by spatial memory deficits measured eight dpi (Fig. 1C). When we analyzed potential sex-dimorphic performances in the tool, we found that female shams performed differently than male sham animals on day seven (Supplemental Fig. 1A), similar to previous reports (Jonasson, 2005). However, no changes were measured when comparing the male and female TBI cohorts on day seven (Supplemental Fig. 1B). No sex-differences were measured when comparing the sham alone or TBI alone during the memory probe on day eight (Supplemental Fig. 1C, D). Examination of gross motor skills revealed that female sham animals swam faster (velocity) and further (total distance traveled) in the open pool than male sham animals (Supplemental Fig. 1E, F). No differences were observed in velocity or distance traveled when comparing the male and female TBI groups (Supplemental Fig. 1E, F). Different performance patterns between male and female shams are likely due to variance in gross motor skills and/or weights. Importantly, performance after moderate, focal trauma is not sex-dependent. These data demonstrate that the unilateral, focal TBI induces spatial learning and memory deficits in both male and female rodents beginning as early as one-week post-injury.

Author Manuscript Author Manuscript Author Manuscript Author Manuscript

2.2. Microglial phagocytic phenotype after trauma

Trauma induces persistent microglial reactivity (reviewed in (Morganti-Kossmann et al., 2019), and recent reports have identified that depletion of microglia can directly impact trauma-induced cognitive deficits (Paladini et al., 2021). Furthermore, increased microglial phagocytosis has been shown to affect obesity-induced cognitive decline (Cope et al., 2018). Here we examined microglial phagocytic phenotype after unilateral focal injury utilizing our newly optimized phagocytosis assay (Krukowski et al., 2018) to assess microglia phagocytic capacity for synapses *in vivo* (Fig. 2A). In this assay, we injected synaptic particles (labeled with fluorescently tagged PSD95, an excitatory post-synaptic marker) into the hippocampi of injured (TBI) animals on day four post-injury (Fig. 2A). Three days later, (7 dpi) microglia were extracted with a percoll gradient from the hemispheres ipsilateral and contralateral to the focal injury. We quantified the number of microglia that engulfed the labeled PSD95-positive synaptic particles by flow cytometry (Fig. 2A). We measured an increase in both the number and percentage of microglia engulfing excitatory synaptic particles from the ipsilateral (injured) hemisphere when compared with microglia from the contralateral (uninjured) hemisphere (Fig. 2B,C). The increase in phagocytic microglia was paralleled by an expansion of the total microglial number (Supplemental Fig. 2) when comparing ipsi- and contralateral hemispheres at seven dpi as previously reported (Morganti et al., 2015; Morganti et al., 2016; Doran et al., 2019; Kumar et al., 2016).

To further explore these *in vivo* findings and define the TBI-induced microglial phagocytic phenotype at nanoscale resolution, we performed ultrastructural analysis by immunocytochemical transmission electron microscopy (immunoTEM) staining against GFP in the CX3CR1-GFP reporter mouse model widely used to visualize microglia. The dorsal CA1 area of the hippocampus is a key region involved in spatial learning and memory (Mumby et al., 2002) and it is sensitive to trauma-induced deficits (Morganti et al., 2015; Morganti-Kossmann et al., 2019). Therefore, we focused immunoTEM analysis in this region on Day 2 and Day 7 post injury (Fig. 3A).

On day two, when comparing the ipsi- to the contralateral hemispheres, we identified an increase in the number of GFP-positive microglia (cells with an electron dense peroxidase immunoprecipitate in their cytoplasm, Fig. 3B) containing cytoplasmic cellular inclusions, defined by the presence of partially digested cellular elements such as mitochondria (Fig. 3B, Table 1). This is indicative of an early step in the phagocytic process prior to complete lysosomal degradation of the cellular elements. At day seven, microglial somata frequently displayed empty endosomes (termed digested vacuoles), indicating that the digestion of cellular elements (initially observed on day 2) had occurred when comparing the ipsi- to the contralateral hippocampi (Table 2). An example of GFP-positive microglial cell body (electron dense precipitate) devoid of cellular inclusions is shown in Fig. 3C. Interestingly, on day two and day seven, some of the microglial cellular inclusions displayed synaptic vesicles indicating their axon terminal nature (Fig. 3D) and mirroring the flow cytometric analysis reported above (Fig. 2). Processes in the contralateral hippocampi instead rarely displayed phagocytic inclusions (Fig. 3E). Other phagocytic parameters investigated by immunoTEM, on day two and day seven, including microglial contact with extracellular debris, lipid bodies, and lipofuscin granules showed no change with TBI (Table 1, Table

Author Manuscript Author Manuscript Author Manuscript Author Manuscript

2). Here we report for the first time that TBI induces a shift in microglial phenotype characterized by an exacerbated phagocytic capacity utilizing two cutting-edge approaches: (i) an *in vivo* microglia phagocytic assay, designed to look specifically at phagocytosis of synaptic elements and (ii) immunoTEM which identifies ultrastructural features of phagocytosis.

2.3. Impact of trauma on synapse loss

Because phagocytic microglia play a role in synapse elimination (Wang et al., 2020), we hypothesized that synaptic number may be reduced in association with the phagocytic microglial phenotype identified with TBI (Figs. 2 and 3). We, therefore, quantified excitatory synapses using flow synaptocytometry (Krukowski et al., 2018; Krukowski et al., 2018). With this technique, intact synapses from isolated hippocampi are labeled with pre- (synapsin-1) and post- (PSD-95) excitatory synaptic markers and quantified by flow cytometry (Fig. 4A). A significant decrease in excitatory synapse number isolated from ipsilateral hippocampi was identified after TBI when compared to sham uninjured animals (Fig. 4B). We found no sex-dependent differences when measuring excitatory synapses from male and female mice after TBI (data not shown). Importantly the loss in excitatory synapse was measured at the same time as the increased phagocytic phenotype observed in microglia.

2.4. Microglial-neuronal interactions after trauma: an increase in satellite microglia

To further shed light on how a phagocytic phenotype in microglia might promote synaptic loss, we investigated the spatial interactions between microglia and neurons in the dorsal hippocampus. Specifically, with immunoTEM, we identified frequent microglial encirclement of neuronal cell bodies in dorsal CA1 after TBI, ipsilateral to the injury (Fig. 5A,B). Microglia cell bodies wrapped around neuronal somata and extended small processes also encircling the soma, sometimes interacting with more than one neuron simultaneously. These interactions were direct contacts, without astrocytic processes or synaptic innervation on the neuronal membrane ensheathed by microglia. These microglia that directly juxtapose neuronal somata have been termed perineuronal ‘satellite’ microglia’ (Savage et al., 2019) and have not been yet characterized after trauma. To further quantify this relationship, we investigated the frequency of satellite microglia using immunofluorescent confocal imaging in transgenic mice with fluorescently labeled excitatory neurons (marked by a genomically encoded mice expressing YFP under the Thy-1 promoter), Fig. 5C. At 7 dpi, brains were extracted and sections containing dorsal CA1 of the hippocampus were stained with antibodies for IBA1 to label microglia. Confocal microscopy followed by 3D reconstruction of excitatory neuronal somata with microglia apposition with Imaris was used. An increase in the percentage of excitatory neurons (denoted in green) with adjacent satellite microglia (denoted in red) was observed when comparing the ipsilateral (representative image Fig. 5D) and contralateral hippocampi (representative image Fig. 5E) in mice exposed to TBI (quantification Fig. 5F). To determine if trauma-induced increases in satellite microglia were specific to excitatory neurons, we discriminated inhibitory neurons with parvalbumin antibodies that are frequently adjacent to the stratum pyramidale of CA1. Satellite microglia (denoted in red) also interacted with the somata of the parvalbumin-expressing (PV +) interneurons (denoted in purple) in CA1 (Fig. 5 D, E). Furthermore, trauma increased

Author Manuscript Author Manuscript Author Manuscript Author Manuscript

the percentage of PV + inhibitory neurons with adjacent satellite microglia (Fig. 5G). Qualitative analysis with immunoTEM in conjunction with quantitative confocal imaging demonstrated that trauma increases the presence of satellite microglia on both excitatory and inhibitory neuron somata.

2.5. Microglial-neuronal interactions after trauma: an increase in synaptic contact

Next, we explored microglial interaction within the dendritic neuronal compartment, a region rich in spines and excitatory synapses, following trauma. At 7 dpi ultrastructural analysis revealed that microglial cell bodies (electron dense material, Fig. 6A) from ipsilateral hippocampi more frequently contacted synaptic elements, including both axon terminals (Fig. 6A) and dendritic spines (Fig. 6A) when compared to the same region in the contralateral hippocampus (Table 2; see Fig. 3E for contralateral example showing typical microglia interacting with synapses). The microglial cell body contacts with dendritic synaptic elements were mediated via short and thick obtuse protrusions (Fig. 6A). In addition, similar to interaction at the soma, microglial processes apposed neuronal dendrites without any axon terminal innervation or astrocytic processes in-between, suggesting that GFP-positive microglial processes might displace excitatory synapses on CA1 dendrites, a process that has been termed synaptic stripping- the physical separation of pre- and post-synaptic elements by microglia (Fig. 6B). No changes were found in microglial contacts with nonsynaptic parts of axons (myelinated fibers) or pockets of extracellular space containing debris (Tables 1 and 2). However, dilation of the microglial endoplasmic reticulum, which is considered a marker of cellular stress, was more often observed at 7dpi (see Fig. 6B for an example, Table 2). The increase in microglial-neuronal interaction at both the soma and the dendrites, as well as the observation of displacement of inhibitory and excitatory synapses in these areas of interaction, support the presence of trauma-induced microglial synaptic stripping (Di Liberto et al., 2018; Chen et al., 2014; Jinno and Yamada, 2011)- an entity not previously associated with TBI. Additional analysis is needed to further characterize this phenomenon in TBI.

2.6. Impact of trauma on inhibitory synaptic input

To investigate the functional correlates of synaptic displacement and phagocytosis by microglia, we examined evoked synaptic input in CA1 pyramidal neurons. Excitatory synaptic drive has been well-established to decrease in CA1 using multiple methods in several models of TBI around this time point (Norris and Scheff, 2009; Almeida-Suhett et al., 2015; Witgen et al., 2005; Schwarzbach et al., 2006). However, the effect of TBI on inhibitory synaptic drive is less clear (Almeida-Suhett et al., 2015; Witgen et al., 2005; Paterno et al., 2017). Parvalbumin-expressing (PV+) interneurons mediate a majority of the somatic inhibition in CA1 (Pelkey et al., 2017). Given that we see an increase in satellite microglia wrapping around the somatic compartment with the displacement of synapses on electron microscopy, we hypothesized that PV-mediated inhibition would be reduced. To test our hypothesis, we evaluated optogenetically evoked, PV+-specific inhibitory synaptic currents (oIPSC) in CA1 pyramidal neurons utilizing acute slices from transgenic mice that express channelrhodopsin exclusively in PV+ neurons (PV-CrexAi32 mice). The oIPSC was recorded in response to a 10 ms flash of blue light at a range of light intensities in slices from both sham and TBI mice (Fig. 7A). oIPSCs were reduced at higher light intensities

Author Manuscript Author Manuscript Author Manuscript Author Manuscript

in neurons from TBI slices compared to sham slices (Fig. 7B,C). Sex-differences in the TBI group for the oIPSC amplitude were not observed (data not shown); however, these experiments were not powered to detect subtle sex-differences and future experiments will be needed. Overall, this reduction in PV-specific inhibitory synaptic drive supports the hypothesis that satellite microglia reduce somatic inhibition.

3. Discussion

Here we provide support for the involvement of a phagocytic microglial phenotype with spatial learning and memory deficits measured one week after contusion injury, as demonstrated both by an *in vivo* phagocytotic assay and ultrastructural analysis with electron microscopy. Ultrastructural analyses revealed microglial inclusions containing synaptic vesicles, at the same timepoints in which synaptic loss was measured. Further examination of spatial interactions demonstrated increased contact of microglia cell bodies with synaptic elements after TBI. Microglia apposed both spines and neuronal somata displacing axonal presynaptic terminals. Interactions were particularly striking with microglia wrapping around neuronal somata in a satellite morphology in the stratum pyramidale. In this same region, reduced PV+-specific, inhibitory synaptic input to pyramidal neurons was measured after TBI. The position of the satellite microglia compiled with the reduced inhibitory input suggests an active role for microglia in circuit reorganization after TBI.

Phagocytosis is a key function of microglia, especially reactive microglia. Our findings of an increased phagocytic microglial phenotype after brain injury are consistent with the literature (Paladini et al., 2021; Morganti-Kossmann et al., 2019). Prior rodent studies investigated trauma-induced microglia reactivity and phagocytosis primarily by microscopic analysis of IBA1 and CD68 antibody expression, on postmortem brain slices (reviewed in (Paladini et al., 2021; Morganti-Kossmann et al., 2019). These reports have demonstrated reactive microglia with increased CD68+ phagolysosomal compartments indicating a phagocytic state post-injury with variations measured depending on the age, sex, and severity of trauma. We demonstrate that trauma-induced microglia changes can be measured *in vivo* utilizing a phagocytic assay in which fluorescently-labeled synapse particles are injected directly into the brain (Krukowski et al., 2018) and confirmed these findings with ultrastructural evaluation. Others have characterized microglia phagocytosis *ex vivo* in culture by measuring bead, myelin, or apoptotic neuronal uptake (Doran et al., 2019; Ritzel et al., 2020). Similar to our *in vivo* findings, Doran *et. al.* found acute increases in phagocytosis in culture at 1 – 3 days post injury (Doran et al., 2019). In a follow-up study, these TBI-induced increases in phagocytic activity lasted eight months post injury in adult, male mice (female mice were not assessed) (Ritzel et al., 2020). At the acute endpoints, microglia phagocytosis was measured by *ex vivo* uptake of fluorescently labeled beads (Doran et al., 2019). However, at the chronic end points there was no longer an increase in bead uptake, but rather *ex vivo* microglia neuronal particle uptake (Ritzel et al., 2020). Acute phagocytic changes in microglia could denote general debris clearance whereas enhanced phagocytosis measured later after injury (7 days – 8 months post injury) might be indicative of a deleterious phenotype. Alternatively, it should not be excluded that assays that utilize bead uptake could be more representative of general phagocytic activity, whereas neuronal

Author Manuscript Author Manuscript Author Manuscript Author Manuscript

uptake assays might target deleterious microglia reactivity. In line with this possibility, our prior study in old mice also identified increases in microglia synapse uptake *in vivo* chronically after TBI associated with memory deficits, while increases in synapse uptake were not measured at earlier endpoints (Krukowski et al., 2018).

Understanding the significance of microglial phagocytosis on neuronal circuit function is of great interest. Given the extensive literature on microglial engulfment of synapses in other conditions, such as development, chronic stress, and neurodegeneration (Tremblay et al., 2010; Schafer et al., 2012; Paolicelli et al., 2011; Gunner et al., 2019; Garber et al., 2019; Hong et al., 2016), it may not be surprising that we found synaptic particles within vesicles of phagocytic microglia after TBI, which is similarly associated with synaptic remodeling and loss. Our finding of synaptic loss is indeed compatible with prior studies, reporting a loss of dendritic spines and excitatory synapses after TBI (Krukowski et al., 2018; Winston et al., 2013; Zhao et al., 2018). Given that enhanced microglia phagocytosis occurred at the same time point in which we measured synapse loss and memory deficits, we hypothesize that at this subchronic timepoint (7 days post injury) the reactive microglia phenotype is deleterious to hippocampal function. However, the exact timing of a deleterious microglia phenotype and the degree of synaptic loss due to microglial-mediated engulfment *versus* secondary to neuronal loss will require further nuanced experimentation. Interestingly, while we found that microglial cell bodies displayed short protrusions after TBI, more proximal microglial cell body processes are specifically associated with increased dendritic spine turnover after contact compared to distal process interaction with spines (Iida et al., 2019).

We dive further into understanding how microglia directly reorganize synapses and circuits after TBI by investigating spatial interactions between microglia and neurons. Further supporting the hypothesis that microglia directly remove synapses after TBI, microglia were intimately associated with synaptic structures at an increased frequency after TBI. Short, obtuse protrusions emanating from the microglial cell body were found to directly contact pre- and post- synaptic structures at the level of synaptic clefts. This may reflect a similar pathological process identified in other injury models, whereby prolongation of microglial contact with presynaptic boutons and extensive wrapping around synaptic structures was found after cerebral ischemia in the somatosensory cortex *in vivo* (Wake et al., 2009) and increased microglial contact with numerous synaptic elements was identified after LPS administration in the CA1 using electron microscopy (Savage et al., 2019). No change in interaction with extracellular debris, suggestive of extracellular digestion or exophagy, an alternative mechanism by which microglia could modify and prune synapses, was found. While we cannot exclude the involvement of trogocytosis (Weinhard et al., 2018), our finding that microglia contact and contain neuronal elements and with ultrastructural features of axon terminals (e.g. synaptic vesicles) suggest that interaction with synaptic elements could be specifically involved.

In addition to increased synaptic interaction at the level of spines, we discovered increased microglial interaction around neuronal somata after TBI. Microglia cell bodies wrapped around neuronal cell bodies, both excitatory and inhibitory neurons, without synaptic innervation in this region of contact. This morphology is congruent with a satellite microglia phenotype, and these data are the first to establish an increase in this type of

Author Manuscript Author Manuscript Author Manuscript Author Manuscript

microglial interaction after TBI. Satellite microglia display spontaneous electrical activity with different characteristics when compared to non-satellite microglia, supporting a unique function for this subtype (Wogram et al., 2016). However, the response of this subset of microglia to pathological states is not well described. Similar to our findings, acute LPS activation increases the number of neurons with associated perineuronal microglia (Chen et al., 2014); axotomy of motor neurons also induces microglial soma attachment to the neuronal cell body along with increasing surface coverage with time (Rotterman and Alvarez, 2020). In normal brains approximately 30% of satellite microglia have processes that entwine around the axon initial segment. While the total number of satellite microglia was not specifically assessed after TBI, contact of these satellite microglial processes with the axonal initial segment decreased at acute time points after TBI (Xiong et al., 2013); suggesting that function of this microglial subtype might change with injury.

A loss of somatic synaptic innervation is associated with satellite microglial interaction. Similar to our findings, both confocal and ultrastructural observations have confirmed a lack of intervening synapses with satellite microglial soma contact in both axotomy and LPS models (Blinzinger and Kreutzberg, 1968; Chen et al., 2014; Rotterman and Alvarez, 2020); and in the cortex, where inhibitory terminals preferentially innervate at the soma and proximal dendrites, the neuronal circumference occupied by pre-synaptic inhibitory boutons was reduced after LPS treatment (Chen et al., 2014). Similarly, in a murine model of encephalitis, IBA1+ phagocytes (interestingly both blood-derived and resident microglia) enwrapped infected neurons in the deep cerebellar nuclei with an associated decrease in inhibitory synapses by immunohistochemistry and a functional reduction of inhibitory input as measured by a decrease in the frequency and amplitude of miniature inhibitory post-synaptic currents (mIPSCs) (Di Liberto et al., 2018). Whether direct phagocytosis of synaptic structures or simply terminal displacement by microglia are needed for reduced somatic innervation remains a controversial area of research (Rotterman and Alvarez, 2020; Rotterman, et al., 2019).

Exploiting optogenetic tools, we also found a link between increased satellite microglia apposition and reduced synaptic inhibition, specifically reduced synaptic inhibition mediated by PV+ interneurons- a subtype of interneurons that innervates the soma (Hu et al., 2014). The current literature regarding the effect of TBI on inhibitory synaptic drive in the hippocampus gives mixed results. While a reduction in the frequency and amplitude of spontaneous and miniature IPSCs, as well as a decrease in the number of GABAergic neurons were identified seven days after a mild controlled cortical impact (Almeida-Suhett et al., 2015), larger evoked and spontaneous IPSCs as well as enhanced GABAergic inhibition in CA1 from cannabinoid-sensitive (presumably cholecystokinin-expressing (CCK+)) interneurons, were noted after lateral fluid percussion injury (Witgen et al., 2005; Johnson et al., 2014). Exploring subtype-specific inhibitory synaptic changes in different TBI models will be required to understand these conflicting results fully. While we measured reduced evoked PV-mediated synaptic inhibition in CA1 pyramidal neurons, several metrics may influence this reduction in addition to a decreased number of pre-synaptic PV+ inhibitory terminals at the soma possibly mediated by microglial stripping, including PV+ neuronal death, axotomy of PV+ neurons, reduced intrinsic excitability of PV+ neurons, changes in pre-synaptic release properties, and modulation of post-synaptic

Author Manuscript Author Manuscript Author Manuscript Author Manuscript

GABA receptors. Additional studies are needed to investigate how microglia might modulate these numerous aspects of the neuronal circuit after TBI. Moreover, it will be important to establish if microglial interactions differentially modulate subtype-specific inputs both onto excitatory and inhibitory neurons.

This study reports microglial phenotypes, microglial-neuronal interactions, and the associated anatomical and functional changes in synapses after TBI, using a multimodal evaluations that widely span from ultrastructural analysis to optogenetic interrogation of circuit function. Our findings elucidate some of the strong interconnection between microglial and synaptic changes after TBI. Future work will investigate the cellular mechanisms of microglial synaptic interaction after brain trauma.

4. Methods

4.1. Animals

All experiments were conducted in accordance with National Institutes of Health (NIH) Guide for the Care and Use of Laboratory Animals and approved by the Institutional Animal Care and Use Committee of the University of California, San Francisco (AN170302; AN184326). Male and female C57B6/J wild-type (WT) mice were received from Jackson Laboratories. Male $CCR2^{RFP/+}$ $CX3CR1^{GFP/+}$, male and female PV-CrexAi32 and male Thy-1-YFP-H (in C57 background) mice were bred inhouse. Mice were 3–5 months of age at the time of surgeries. Animal shipments were received at least one week prior to start of experimentation to allow animals to habituate to the new surroundings. Mice were group housed (by sexes and injury state) in environmentally controlled conditions with a reverse light cycle (12:12 h light: dark cycle at 21 ± 1 °C; ~50% humidity) and provided food and water ad libitum.

4.2. Surgeries

All animals were randomly assigned to each TBI or sham surgery groups. Animals were anesthetized and maintained at 2–2.5% isoflurane. Controlled Cortical Impact (CCI) surgery was performed as previously described (Krukowski et al., 2020; Chou et al., 2017; Chou et al., 2018; Krukowski et al., 2018). Briefly, mice were secured to a stereotaxic frame with nontraumatic ear bars. A midline incision exposed the skull followed by a ~3.5-mm diameter craniectomy and removal of part of the skull, using an electric microdrill. The coordinates of the craniectomy were: anteroposterior, −2.00 mm and mediolateral, +2.00 mm with respect to bregma. Any animal that experienced excessive bleeding due to disruption of the dura was removed from the study. After the craniectomy, the removed skull was discarded and the contusion was induced using a 3-mm convex tip attached to an electromagnetic impactor (Leica). The contusion depth was set to 0.95 mm from dura with a velocity of 4.0 m/s sustained for 300 ms. Following impact, the scalp was sutured. These injury parameters were chosen to target, but not penetrate, the hippocampus. Sham animals were subjected to identical parameters excluding the craniectomy and impact. Post surgery, the mice recovered in an incubation chamber set to 37 °C for ~30 min until animals displayed normal walking and grooming behavior (at which point animals were returned to their home cage). All animals fully recovered from the surgical procedures as exhibited by normal

Author Manuscript Author Manuscript Author Manuscript Author Manuscript

behavior, healed sutures, and weight maintenance monitored throughout the duration of the experiments.

4.3. Radial arm water maze

The radial arm water maze (RAWM) was used to test spatial learning and memory in rodents (Chou et al., 2017; Alamed et al., 2006; Krukowski et al., 2020). The pool is 118.5 cm in diameter with 8 arms, each 41 cm in length, and an escape platform. The escape platform is slightly submerged below the water level, so it is not visible to the animals. The pool was filled with water that was rendered opaque by adding white paint (Crayola, 54–2128–053). Visual cues are placed around the room such that they were visible to animals exploring the maze. Mice performed 9 trials on the learning day (day 7), every three trials were averaged for 1 block (3 blocks total were run on day 7). One block (3 trials) during the memory probe (day 8). On both learning and memory days there is a 10-minute inter-trial interval. During a trial, animals were placed in a random arm that did not include the escape platform. Animals were allowed 1 min to locate the escape platform. On successfully finding the platform, animals remained there for 10 s before being returned to their warmed, holding cage. On a failed trial, animals were guided to the escape platform and then returned to their holding cage 10 s later. The escape platform location was the same, whereas the start arm varied between trials. RAWM data were collected through a video tracking and analysis setup (Ethovision XT 8.5, Noldus Information Technology). The program automatically analyzed the number of entries into non-target arms made per trial. Every three trials were averaged into a block to account for large variability in performance; the learning day consisted of 3 blocks, whereas each memory test was one block.

4.4. In vivo microglia phagocytic assay

Microglia isolation and flow cytometry analyses were done as previously described with modifications (Krukowski et al., 2018). Mice were lethally overdosed, animals were perfused with ice cold PBS and hemibrains were collected. Briefly, fresh brains were digested into single cell suspension using the Neural Tissue Dissociation kit (P) (Miltenyi Biotec) according to the manufacturer's instructions. After washing with cold HBSS, cells were then resuspended in 30% percoll solution (Sigma-Aldrich, Inc.) and centrifuged at 800g for 20 min. Cell pellets were collected, washed and stained with BV711-CD45 and AF700-CD11b antibodies before analyzing with an Aria III sorter (BD). For the phagocytosis assay, 10μg enriched synaptosomes were stained with PSD-95 antibody (1:200, Abcom, ab13552), washed, stained with secondary antibody (1:400, goat anti-mouse 488 Invitrogen, Carlsbad, CA A31556), washed again and resuspended in 100 μl sterile PBS before injection. 2 μl pre-stained synaptosomes were injected into the right hippocampus using the following coordinate, bregma, AP − 1.6 mm, LR + 1.6 mm and DV − 2mm. Mice were euthanized three days post injection and right hemispheres were used for flow cytometry analysis as described above. Data were analyzed in Flowjo™ software (v10, Tree Star Inc.). At least 2,000 microglia cells ($CD45^{low}$ $CD11b^{+}$ events) were collected for the analysis.

Author Manuscript Author Manuscript Author Manuscript Author Manuscript

4.5. ImmunoTEM

4.5.1. Perfusion—Adult (3–5 months of age) male CCR2$^{RFP/+}$ CX3CR1$^{GFP/+}$ mice were anesthetized with a mixture of ketamine (10 mg/ml) and xylaxine (1 mg/ml) and transcardially perfused with cold phosphate-buffered saline (PBS; 50 mM at pH 7.4) followed by 250 ml of glutaraldehyde 0.2%/PFA 4% diluted in phosphate buffer (PB, 100 mM at pH 7.4). Fifty-micron thick coronal sections of the brain were cut in PBS using a vibratome (Leica VT1000S) and stored in cryoprotectant at − 20 °C. Considering the time-consuming nature of the electron microscopy experiments, and the fact that no difference between male and female mice were measured in the memory deficits, only male mice were used.

4.5.2. Immunostaining—Brain sections containing the dorsal hippocampus CA1 from Bregma − 1.43 mm to − 2.27 mm (The mouse brain in stereotaxic coordinates, Paxinos and Franklin, 4th edition) were selected for immunoperoxidase staining for electron microscopy, performed as previously described (El Hajj et al., 2019). Briefly, sections were washed in PBS, quenched with 0.3% hydrogen peroxide followed by PBS wash and incubation in 0.1% solution of $NaBH_4$. Sections were rinsed in PBS and incubated for 2 h in blocking buffer (10% normal serum, 3% bovine serum albumin and 0.01% Triton X-100), followed by overnight incubation with primary antibody (chicken anti-GFP, 1:5000, Aves Labs, GFP-1020). Following TBS rinse, sections were incubated with the appropriate secondary antibodies conjugated to biotin (1:300 in TBS; Jackson Immunoresearch) and revealed with diaminobenzidine (DAB, 0.05%) in 0.015% hydrogen peroxide for 3 to 6 min. Sections were post-fixed in 1% osmium tetroxide, dehydrated using sequential alcohol baths followed by propylene oxide. Sections were impregnated with Durcupan resin (Sigma-Aldrich Canada Ltd.) overnight at RT, and polymerized between ACLAR films (Electron Microscopy Sciences; EMS) at 55 °C for 72 h. Small regions of interest (CA1 containing pyramidal cell layer and *stratum radiatum*) were excised, glued to resin blocks, and 70–80 nm sections were collected onto thin mesh grids (EMS) for transmission electron microscopy using an ultramicrotome (Leica UC7).

4.5.3. Transmission Electron Microscopy—The ultrathin sections were imaged using a FEI Tecnai G2 Spirit Biotwin microscope with a digital camera ORCA-HR (10MP; Hamamatsu, Japan). The qualitative analysis focused on both the CA1 pyramidal cell layer and *stratum radiatum*, and the quantitative analysis focusing on interactions with the synaptic neuropil on the *stratum radiatum.* Microglia cell bodies and their processes were identified by their GFP immunoreactivity. Pictures of microglial cell bodies were randomly acquired at a magnification of x4800 for the cell bodies and of x6800 for the processes, capturing all the immunopositive elements that were not partially hidden by a grid bar or a contaminant, for instance, to avoid introducing bias. Quantitative analysis of microglial cell bodies was performed blind to the experimental conditions in the CA1 *stratum radiatum* with ImageJ software (n = 16–17 microglia/group), using well-defined ultrastructural identification criteria summarized in detail in (Nahirney and Tremblay, 2021). In particular, microglial cellular inclusions, digested vacuoles, lipid bodies, lipofuscin granules, and dilated endoplasmic reticulum or Golgi apparatus cisternae were analyzed, counting the number of each subcellular element within each microglial cell body analyzed

Author Manuscript Author Manuscript Author Manuscript Author Manuscript

(El Hajj et al., 2019). Cellular inclusions were defined as endosomes containing cellular elements (including axon terminals with distinctive synaptic vesicles, but also elements that were in a more advanced stage of digestion and hence not recognizable) at various stages of digestion. Digested vacuoles had a fully lucent contact and were larger than 300 nm (Savage et al., 2020). Dilation of the endoplasmic reticulum and/or Golgi apparatus cisternae was noted when the distance between the cisternal membranes was 50 nm or greater (El Hajj et al., 2019; Hui et al., 2018). Microglial contacts with myelinated axons, extracellular debris, and synapses between presynaptic axon terminals and post-synaptic dendritic spines were also quantified, for each microglial cell body analyzed. In particular, presynaptic axon terminals were differentiated by their synaptic vesicles, while post-synaptic spines were in contact with a pre-synaptic axon terminal, often with a visible post-synaptic density at their junction (El Hajj et al., 2019; Hui et al., 2018). In addition, in our qualitative analysis, neuronal cell bodies were distinguished by their pale nuclei and pale cytoplasm, heterochromatin pattern, as well as innervation from axon terminals (El Hajj et al., 2019; Hui et al., 2018).

4.5.4. Flow Synaptocytometry—Flow synatocytometry was performed as previously described (Krukowski et al., 2018; Krukowski et al., 2018). Hippocampi were homogenized in 0.32 M sucrose in HEPES (Sigma Aldrich, St. Louis, MO H0887) in a glass Dounce homogenizer. Gross tissue fragments were removed in a by centrifugation (1200×g for 10 min), supernatant collected. Synaptosomes were isolated by further centrifugation (13000×g for 20 min), supernatant was discarded and pellets containing synaptosomes were collected. Samples are kept cold (either on ice or in chilled centrifuges) for staining procedures. Synaptosome collection was standardized between samples will be by total protein concentrations (Pierce BCA Protein Assay, Thermo Scientific, Rockford, IL, 23225). Synaptosomes (50 μg/ml) were divided into 1.5 ml microcentrifuge tubes for staining. For antibody staining, synaptosomes were first permeabilized by Cytofix/Cytoperm fixation solution (BD Biosciences, San Diego, CA, 554722) for 20 min on ice. Samples were washed 2x with 700 μl of perm/wash buffer (BD Biosciences, San Diego, CA, 554723) at 13,000 × g for 5 min. at 4 °C. Primary antibodies (Synapsin-1 and PSD-95) were added for 30 min and agitated after 15 min. Samples were washed 2x with 700 μl of perm/wash buffer at 13,000×g for 5 min. at 4 °C. Secondary antibodies (Goat anti-rabbit 405, Invitrogen, Carlsbad, CA A31556; Goat anti-mouse 488 Invitrogen, Carlsbad, CA, A11001; Goat anti-mouse 647 Invitrogen, Carlsbad, CA, A21236) were added for 30 min and agitated after 15 min at 4 °C in the dark. All reagents were made fresh for each staining day. Synaptosomes were determined by size-calibrated beads and co-staining with antibodies specific for pre (synapsin-1) and post-synaptic (PSD-95) markers. No positive staining was observed in samples containing: (1) no synaptosomes (2) secondary antibodies alone. Samples were run in duplicate or triplicate. Data were collected on an LSRII (BD) and analyzed with Flowjo™ software (v10, Tree Star Inc.). 30,000 events were collected for total synaptosomes.

4.5.5. Immunofluorescent Confocal Imaging—For immunohistochemistry analysis, animals were lethally overdosed, followed by PBS perfusion, brains were fixed in ice-cold 4% paraformaldehyde, pH 7.5 (PFA, Sigma Aldrich, St. Louis, MO, 441244) for 24 hrs followed by sucrose (Fisher Science Education, Nazareth, PA, S25590A) protection (15% to

Author Manuscript Author Manuscript Author Manuscript Author Manuscript

30%). Brains were sectioned into 20 μm slices using a Leica cryostat (Leica Microsystems, Wetzlar, Germany) and mounted on slides (ThermoFisher Scientific, South San Francisco, CA). Slides were brought to room temperature (20 °C) prior to use. Slides were washed three times with tris-buffered saline (TBS) for 10 min. each. All slides were blocked in a 10% donkey serum diluted in 0.1 M phosphate buffered saline (PBS) with 0.5% Triton X-100 for 1 h in the dark. Slides were then stained with primary antibodies specific for Iba-1 (Rabbit, Wako, Richmond, VA 019–19741, 1:500) and parvalbumin (Mouse, Millipore, MAB1572, 1:5000) overnight, washed three times in TBS, and stained for the secondary antibody, donkey anti-rabbit Alexa-555 (Invitrogen, Carlsbad, CA, A31572, 1:500) and donkey anti-mouse Alexa-647 (Abcam, Cambridge, UK, 181292, 1:500). Tissues were fixed using ProLong Gold (Invitrogen, Carlsbad, CA, P36930) and a standard slide cover sealed with nail polish. 3–4 images separated by 100–140 μm in CA1 dorsal hippocampus were averaged per animal. 15 μm in depth z-stack images were acquired on a Nikon High Speed Widefield Confocal microscope (Ti inverted fluorescence; CSU-W1) at the UCSF Nikon Imaging Center. 200x magnification.

4.5.6. Imaris Analysis—Imaris v.9.6 was utilized for 3D visualization of confocal data (Bitplane, http://www.bitplane.com/imaris). The 3D view tab in the Imaris imaging software was used to optimize brightness, contrast and 3D-rendering properties for the best representation of the imaging. Due to variations in Thy-1 brightness contralateral and ipsilateral brains were paired for generating the best parameters. 3D reconstruction of excitatory neuronal somas (Thy1-YFP), parvalbumin-expressing inhibitory neuronal somas (Parvalbumin+, Alexa-647) and microglia (Iba1+, Alexa-555) were generated in the Imaris Surface modality. Satellite microglia were calculated as microglia that were directly touching a neuronal soma (distance from soma = 0).

4.5.7. Electrophysiology—Acute sagittal brain slices (250 μm) including the hippocampus were prepared from mice that underwent either TBI or sham surgical procedures 7–9 days prior (n = 4 mice per group). Mice were anesthetized with Euthasol (0.1 ml / 25 g, Virbac, Fort Worth, TX, NDC-051311–050–01), and transcardially perfused with an ice-cold sucrose cutting solution containing (in mM): 210 sucrose, 1.25 NaH_2PO_4, 25 $NaHCO_3$, 2.5 KCl, 0.5 $CaCl_2$, 7 $MgCl_2$, 7 dextrose, 1.3 ascorbic acid, 3 sodium pyruvate (bubbled with 95% O_2 – 5% CO_2, pH 7.4) Mice were then decapitated and the brain was isolated in the same sucrose solution and cut on a slicing vibratome (Leica, VT1200S, Leica Microsystems, Wetzlar, Germany). Slices were incubated in a holding solution (composed of (in mM): 125 NaCl, 2.5 KCl, 1.25 NaH_2PO_4, 25 $NaHCO_3$, 2 $CaCl_2$, 2 $MgCl_2$, 10 dextrose, 1.3 ascorbic acid, 3 sodium pyruvate, bubbled with 95% O_2 – 5% CO_2, pH 7.4) at 36 °C for 30 min and then at room temperature for at least 30 min until recording.

Whole cell voltage clamp recordings were obtained from these slices in a submersion chamber with a heated (32 – 34 °C) artificial cerebrospinal fluid (aCSF) containing (in mM): 125 NaCl, 3 KCl, 1.25 NaH_2PO_4, 25 $NaHCO_3$, 2 $CaCl_2$, 1 $MgCl_2$, 10 dextrose (bubbled with 95% O_2 – 5% CO_2, pH 7.4). Patch pipettes (3–6 MΩ) were manufactured from filamented borosilicate glass capillaries (Sutter Instruments, Novato, CA, BF100–58-10) and filled with an intracellular solution containing (in mM): 135 CsMeS, 5 CsCl, 10 HEPES, 4

Author Manuscript Author Manuscript Author Manuscript Author Manuscript

NaCl, 4 MgATP, 0.3 Na3GTP, 7 2 K-phosphcreatine, 2 Qx314Br, and 1–2% biocytin. CA1 pyramidal neurons were identified using infrared microscopy with a 40x waterimmersion objective (Olympus, Burlingame, CA). Recordings were made using a Multiclamp 700B (Molecular Devices, San Jose, CA) amplifier, which was connected to the computer with a Digidata 1440A ADC (Molecular Devices, San Jose, CA), and recorded at a sampling rate of 20 kHz with pClamp software (Molecular Devices, San Jose, CA). We did not correct for the junction potential, but access resistance and pipette capacitance were appropriately compensated before each recording.

To measure optogenetically-evoked PV+-mediated post synaptic currents (oIPSC) in CA1 pyramidal neurons, the cell was held at 0 mV in voltage clamp. 10 msec flashes of blue light, generated by a Lambda DG-4 high-speed optical switch with a 300 W Xenon lamp (Sutter Instruments) and an excitation filter set centered around 470 nm, were delivered to the slice through a 40x objective (Olympus) with a range of light intensities from 40 uW to 4 mW. At each light intensity, the light pulse was repeated five times with 30 sec intervals in between each stimulus. The five oIPSCs were averaged and peak amplitude measured for each light intensity.

4.5.8. Statistics—All data were evaluated with GraphPad Prism 8 statistical software. Statistical significance between groups for most variables was determined using a Student two-tailed *t*-test with or without Welch's correction. For nonparametric data, including the electron microscopy analyses, a Mann-Whitney-test was assessed to determine significance. The RAWM maze and the oIPSC amplitude with increasing light intensity were analyzed as a repeated measures two way ANOVA with a Bonferroni post hoc examination. Outliers were determined using the ROUT method in GraphPad Prism with Q (the maximum desired false discovery rate) set at 2%. Only one outlier was identified in the optogenetically-evoked inhibitory postsynaptic current data which was excluded from the analysis. P values below 0.05 were considered significant. Individual statistical analysis is denoted in the figure legends.

The number of mice used was sufficient to result in statistically significant differences using standard power calculations with alpha = 0.05 and a power of 0.8. We used an online tool (http://www.bu.edu/orccommittees/iacuc/policies-and-guidelines/sample-size-calculations/) to calculate power and samples size based on experience with the respective tests, variability of the assays and inter-individual differences within groups. All experiments were randomized and blinded by an independent researcher to injury group.

Supplementary Material

Refer to Web version on PubMed Central for supplementary material.

Acknowledgement

We are grateful to Dr. Sachiko Sato and Julie-Christine Lévesque at the Bioimaging Platform of Centre de recherche du CHU de Québec-Université Laval, as well as Audrey Gagné for her help with electron microscopy imaging and Maude Bordeleau for her help with statistical analyses. Microscopic images were obtained at the Nikon Imaging Center at UCSF. Schematic diagrams in figures created in Biorender.com.

Author Manuscript Author Manuscript Author Manuscript Author Manuscript

Funding

This work was supported by the NIH/National Institute on Aging Grant R01AG056770 (to S.R.), the NIH/National Cancer Institute Grant R01 R01CA246722 (to S.R), the NRSA post-doctoral fellowship from the NIA F32AG054126 (to K.K), the National Institute for General Medicine (NIGMS) Initiative for Maximizing Student Development (R25GM056847) and the National Science Foundation (NSF) Graduate Fellowship Program (To E.S.F), the UCSF Clinical and National Center for Advanced Translational Sciences at NIH (UCSF-CTSI Grant Number TL1 TR001871) and the NIH/NINDS (K08NS114170) (To A.N). K.P. was supported by a doctoral scholarship from Fonds de recherche du Québec – Santé, an excellence award from Fondation du CHU de Québec, as well as from Centre thématique de recherche en neurosciences and from Fondation Famille-Choquette. This study was funded by a Canadian Institutes of Health Research Foundation Grant (148420) and Natural Sciences and Engineering Research Council of Canada (NSERC) Discovery grant (RGPIN-2014–05308) awarded to M.E.T. M.E.T. is a Tier II Canada Research Chair in Neurobiology of Aging and Cognition. The San Francisco General Hospital Flow Core Facility was supported by the National Institutes of Health (P30 AI027763).

References

Tremblay M-È, Lowery RL, Majewska AK, Dalva M, 2010. Microglial interactions with synapses are modulated by visual experience. PLoS Biol. 8 (11), e1000527. [PubMed: 21072242]

Li Y, Du XF, Liu CS, Wen ZL, Du JL, 2012. Reciprocal regulation between resting microglial dynamics and neuronal activity in vivo. Dev. Cell 23, 1189–1202. [PubMed: 23201120]

Schafer D, et al. , 2012. Microglia sculpt postnatal neural circuits in an activity and complement-dependent manner. Neuron 74 (4), 691–705. [PubMed: 22632727]

Parkhurst C, et al. , 2013. Microglia promote learning-dependent synapse formation through brain-derived neurotrophic factor. Cell 155 (7), 1596–1609. [PubMed: 24360280]

Badimon A, et al. , 2020. Negative feedback control of neuronal activity by microglia. Nature 586 (7829), 417–423. [PubMed: 32999463]

Bennett MR, 2007. Synaptic P2X7 receptor regenerative-loop hypothesis for depression. Aust. N. Z. J. Psychiatry 41 (7), 563–571. [PubMed: 17558618]

Tremblay ME, Majewska AK, 2011. A role for microglia in synaptic plasticity? Commun. Integr. Biol. 4, 220–222. [PubMed: 21655446]

Schafer DP, Lehrman EK, Stevens B, 2013. The “quad-partite” synapse: microglia-synapse interactions in the developing and mature CNS. Glia 61 (1), 24–36. [PubMed: 22829357]

Paolicelli RC, Bolasco G, Pagani F, Maggi L, Scianni M, Panzanelli P, Giustetto M, Ferreira TA, Guiducci E, Dumas L, Ragozzino D, Gross CT, 2011. Synaptic pruning by microglia is necessary for normal brain development. Science 333 (6048), 1456–1458. [PubMed: 21778362]

Gunner G, et al. , 2019. Sensory lesioning induces microglial synapse elimination via ADAM10 and fractalkine signaling. Nat. Neurosci. 22 (7), 1075–1088. [PubMed: 31209379]

Weinhard L, et al. , 2018. Microglia remodel synapses by presynaptic trogocytosis and spine head filopodia induction. Nat. Commun. 9 (1) 10.1038/s41467-018-03566-5.

Blinzinger K, Kreutzberg G, 1968. Displacement of synaptic terminals from regenerating motoneurons by microglial cells. Z Zellforsch Mikrosk Anat 85 (2), 145–157. [PubMed: 5706753]

Trapp BD, Wujek JR, Criste GA, Jalabi W, Yin X, Kidd GJ, Stohlman S, Ransohoff R, 2007. Evidence for synaptic stripping by cortical microglia. Glia 55 (4), 360–368. [PubMed: 17136771]

Akiyoshi R, et al. , Microglia Enhance Synapse Activity to Promote Local Network Synchronization. eNeuro 5, (2018).

Nagamoto-Combs K, McNeal DW, Morecraft RJ, Combs CK, 2007. Prolonged microgliosis in the rhesus monkey central nervous system after traumatic brain injury. J. Neurotrauma 24 (11), 1719–1742. [PubMed: 18001202]

Ramlackhansingh AF, et al. , 2011. Inflammation after trauma: microglial activation and traumatic brain injury. Ann. Neurol. 70 (3), 374–383. [PubMed: 21710619]

Johnson VE, Stewart JE, Begbie FD, Trojanowski JQ, Smith DH, Stewart W, 2013. Inflammation and white matter degeneration persist for years after a single traumatic brain injury. Brain 28–42. [PubMed: 23365092]

Author Manuscript Author Manuscript Author Manuscript Author Manuscript

Morganti JM, et al. , 2015. CCR2 Antagonism Alters Brain Macrophage Polarization and Ameliorates Cognitive Dysfunction Induced by Traumatic Brain Injury. J. Neurosci. 35 (2), 748–760. [PubMed: 25589768]

Loane DJ, Kumar A, 2016. Microglia in the TBI brain: The good, the bad, and the dysregulated. Exp. Neurol. 275 (Pt 3), 316–327. [PubMed: 26342753]

Donat CK, Scott G, Gentleman SM, Sastre M, 2017. Microglial Activation in Traumatic Brain Injury. Front. Aging Neurosci. 9, 208. [PubMed: 28701948]

Paladini MS, Feng X, Krukowski K, Rosi S, 2021. Microglia depletion and cognitive functions after brain injury: From trauma to galactic cosmic ray. Neurosci. Lett. 741, 135462. 10.1016/j.neulet.2020.135462. [PubMed: 33259927]

Xiong Y, Mahmood A, Chopp M, 2013. Animal models of traumatic brain injury. Nat. Rev. Neurosci. 14 (2), 128–142. [PubMed: 23329160]

Chou A, et al. , 2017. Inhibition of the integrated stress response reverses cognitive deficits after traumatic brain injury. Proc. Natl. Acad. Sci. U. S. A. 114 (31), E6420–E6426. [PubMed: 28696288]

Chou A, Krukowski K, Morganti J, Riparip L-K, Rosi S, 2018. Persistent Infiltration and Impaired Response of Peripherally-Derived Monocytes after Traumatic Brain Injury in the Aged Brain. Int. J. Mol. Sci. 19 (6), 1616. 10.3390/ijms19061616.

Krukowski K, et al. , 2018. Traumatic Brain Injury in Aged Mice Induces Chronic Microglia Activation, Synapse Loss, and Complement-Dependent Memory Deficits. Int. J. Mol. Sci. 19 (12), 3753. 10.3390/ijms19123753.

Alamed J, Wilcock DM, Diamond DM, Gordon MN, Morgan D, 2006. Two-day radial-arm water maze learning and memory task; robust resolution of amyloid-related memory deficits in transgenic mice. Nat. Protoc. 1 (4), 1671–1679. [PubMed: 17487150]

McAllister TW, et al. , 2001. Differential working memory load effects after mild traumatic brain injury. Neuroimage 14 (5), 1004–1012. [PubMed: 11697932]

Palacios EM, et al. , 2012. White matter integrity related to functional working memory networks in traumatic brain injury. Neurology 78 (12), 852–860. [PubMed: 22345222]

Manktelow AE, Menon DK, Sahakian BJ, Stamatakis EA, 2017. Working memory after traumatic brain injury: the neural basis of improved performance with methylphenidate. Front. Behav. Neurosci. 11, 58. [PubMed: 28424597]

Jonasson Z, 2005. Meta-analysis of sex differences in rodent models of learning and memory: a review of behavioral and biological data. Neurosci. Biobehav. Rev. 28 (8), 811–825. [PubMed: 15642623]

Morganti-Kossmann MC, Semple BD, Hellewell SC, Bye N, Ziebell JM, 2019. The complexity of neuroinflammation consequent to traumatic brain injury: from research evidence to potential treatments. Acta Neuropathol. 137 (5), 731–755. [PubMed: 30535946]

Cope EC, et al. , 2018. Microglia Play an Active Role in Obesity-Associated Cognitive Decline. J. Neurosci. 38 (41), 8889–8904. [PubMed: 30201764]

Morganti JM, Riparip L-K, Rosi S, Borlongan CV, 2016. Call Off the Dog(ma): M1/ M2 Polarization Is Concurrent following Traumatic Brain Injury. PLoS ONE 11 (1), e0148001. [PubMed: 26808663]

Doran SJ, et al. , 2019. Sex differences in acute neuroinflammation after experimental traumatic brain injury are mediated by infiltrating myeloid cells. J. Neurotrauma 36 (7), 1040–1053. [PubMed: 30259790]

Kumar A, Alvarez-Croda D-M, Stoica BA, Faden AI, Loane DJ, 2016. Microglial/Macrophage Polarization Dynamics following Traumatic Brain Injury. J. Neurotrauma 33 (19), 1732–1750. [PubMed: 26486881]

Mumby DG, Gaskin S, Glenn MJ, Schramek TE, Lehmann H, 2002. Hippocampal damage and exploratory preferences in rats: memory for objects, places, and contexts. Learn Mem 9, 49–57. [PubMed: 11992015]

Wang C, Yue H, Hu Z, Shen Y, Ma J, Li J, Wang X-D, Wang L, Sun B, Shi P, Wang L, Gu Y, 2020. Microglia mediate forgetting via complement-dependent synaptic elimination. Science 367 (6478), 688–694. [PubMed: 32029629]

Author Manuscript Author Manuscript Author Manuscript Author Manuscript

Krukowski K, Grue K, Frias ES, Pietrykowski J, Jones T, Nelson G, Rosi S, 2018. Female mice are protected from space radiation-induced maladaptive responses. Brain Behav. Immun. 74, 106–120. [PubMed: 30107198]

Savage JC, Carrier M, Tremblay ME, 2019. Morphology of microglia across contexts of health and disease. Methods Mol. Biol. 2034, 13–26. [PubMed: 31392674]

Di Liberto G, et al. , 2018. Neurons under T cell attack coordinate phagocyte-mediated synaptic stripping. Cell 175 (2), 458–471.e19. [PubMed: 30173917]

Chen Z, et al. , 2014. Microglial displacement of inhibitory synapses provides neuroprotection in the adult brain. Nat. Commun. 5 (1) 10.1038/ncomms5486.

Jinno S, Yamada J, 2011. Using comparative anatomy in the axotomy model to identify distinct roles for microglia and astrocytes in synaptic stripping. Neuron Glia Biol 7 (1), 55–66. [PubMed: 22217547]

Norris CM, Scheff SW, 2009. Recovery of afferent function and synaptic strength in hippocampal CA1 following traumatic brain injury. J. Neurotrauma 26 (12), 2269–2278. [PubMed: 19604098]

Almeida-Suhett CP, et al. , 2015. GABAergic interneuronal loss and reduced inhibitory synaptic transmission in the hippocampal CA1 region after mild traumatic brain injury. Exp. Neurol. 273, 11–23. [PubMed: 26238734]

Witgen BM, et al. , 2005. Regional hippocampal alteration associated with cognitive deficit following experimental brain injury: a systems, network and cellular evaluation. Neuroscience 133 (1), 1–15. [PubMed: 15893627]

Schwarzbach E, Bonislawski DP, Xiong G, Cohen AS, 2006. Mechanisms underlying the inability to induce area CA1 LTP in the mouse after traumatic brain injury. Hippocampus 16 (6), 541–550. [PubMed: 16634077]

Paterno R, Folweiler KA, Cohen AS, 2017. Pathophysiology and treatment of memory dysfunction after traumatic brain injury. Curr. Neurol. Neurosci. Rep. 17, 52. [PubMed: 28500417]

Pelkey KA, Chittajallu R, Craig MT, Tricoire L, Wester JC, McBain CJ, 2017. Hippocampal GABAergic inhibitory interneurons. Physiol. Rev. 97 (4), 1619–1747. [PubMed: 28954853]

Ritzel RM, et al. , 2020. Sustained neuronal and microglial alterations are associated with diverse neurobehavioral dysfunction long after experimental brain injury. Neurobiol. Dis. 136, 104713. 10.1016/j.nbd.2019.104713. [PubMed: 31843705]

Garber C, et al. , 2019. T cells promote microglia-mediated synaptic elimination and cognitive dysfunction during recovery from neuropathogenic flaviviruses. Nat. Neurosci. 22 (8), 1276–1288. [PubMed: 31235930]

Hong S, et al. , 2016. Complement and microglia mediate early synapse loss in Alzheimer mouse models. Science 352 (6286), 712–716. [PubMed: 27033548]

Winston CN, et al. , 2013. Controlled cortical impact results in an extensive loss of dendritic spines that is not mediated by injury-induced amyloid-beta accumulation. J. Neurotrauma 30 (23), 1966–1972. [PubMed: 23879560]

Zhao J, et al. , 2018. Mild traumatic brain injury reduces spine density of projection neurons in the medial prefrontal cortex and impairs extinction of contextual fear memory. J. Neurotrauma 35 (1), 149–156. [PubMed: 28665166]

Iida T, Tanaka S, Okabe S, 2019. Spatial impact of microglial distribution on dynamics of dendritic spines. Eur. J. Neurosci. 49 (11), 1400–1417. [PubMed: 30585660]

Wake H, Moorhouse AJ, Jinno S, Kohsaka S, Nabekura J, 2009. Resting microglia directly monitor the functional state of synapses in vivo and determine the fate of ischemic terminals. J. Neurosci. 29 (13), 3974–3980. [PubMed: 19339593]

Savage JC, St-Pierre MK, Hui CW, Tremblay ME, 2019. Microglial Ultrastructure in the Hippocampus of a Lipopolysaccharide-Induced Sickness Mouse Model. Front. Neurosci. 13, 1340. [PubMed: 31920505]

Wogram E, et al. , 2016. Satellite microglia show spontaneous electrical activity that is uncorrelated with activity of the attached neuron. Eur. J. Neurosci. 43 (11), 1523–1534. [PubMed: 27060918]

Rotterman TM, Alvarez FJ, 2020. Microglia dynamics and interactions with motoneurons axotomized after nerve injuries revealed by two-photon imaging. Sci. Rep. 10, 8648. [PubMed: 32457369]

Author Manuscript Author Manuscript Author Manuscript Author Manuscript

Rotterman TM et al. , Spinal motor circuit synaptic plasticity after peripheral nerve injury depends on microglia activation and a CCR2 mechanism. J. Neurosci, 39, 3412–3433 (2019). [PubMed: 30833511]

Hu H, Gan J, Jonas P, 2014. Interneurons. Fast-spiking, parvalbumin(+), GABAergic interneurons: from cellular design to microcircuit function. Science 345, 1255263. [PubMed: 25082707]

Johnson BN, et al. , 2014. Augmented inhibition from cannabinoid-sensitive interneurons diminishes CA1 output after traumatic brain injury. Front. Cell. Neurosci. 8 10.3389/fncel.2014.00435.

Krukowski K, et al. , 2020. Integrated stress response inhibitor reverses sex-dependent behavioral and cell-specific deficits after mild repetitive head trauma. J. Neurotrauma 37 (11), 1370–1380. [PubMed: 31884883]

Krukowski K, et al. , 2020. Small molecule cognitive enhancer reverses age-related memory decline in mice. Elife 9. 10.7554/eLife.62048.

Krukowski K, et al. , 2018. Temporary microglia-depletion after cosmic radiation modifies phagocytic activity and prevents cognitive deficits. Sci. Rep. 8 (1) 10.1038/s41598-018-26039-7.

El Hajj H, et al. , 2019. Ultrastructural evidence of microglial heterogeneity in Alzheimer's disease amyloid pathology. J. Neuroinflammation 16 (1). 10.1186/s12974-019-1473-9.

Nahirney PC, Tremblay ME, 2021. Brain ultrastructure: putting the pieces together. Front. Cell Dev. Biol. 9.

Savage JC, et al. , 2020. Microglial physiological properties and interactions with synapses are altered at presymptomatic stages in a mouse model of Huntington's disease pathology. J Neuroinflammation 17 (1). 10.1186/s12974-020-01782-9.

Hui CW, et al. , 2018. Nonfunctional mutant Wrn protein leads to neurological deficits, neuronal stress, microglial alteration, and immune imbalance in a mouse model of Werner syndrome. Brain Behav. Immun. 73, 450–469. [PubMed: 29908963]

Author Manuscript Author Manuscript Author Manuscript Author Manuscript

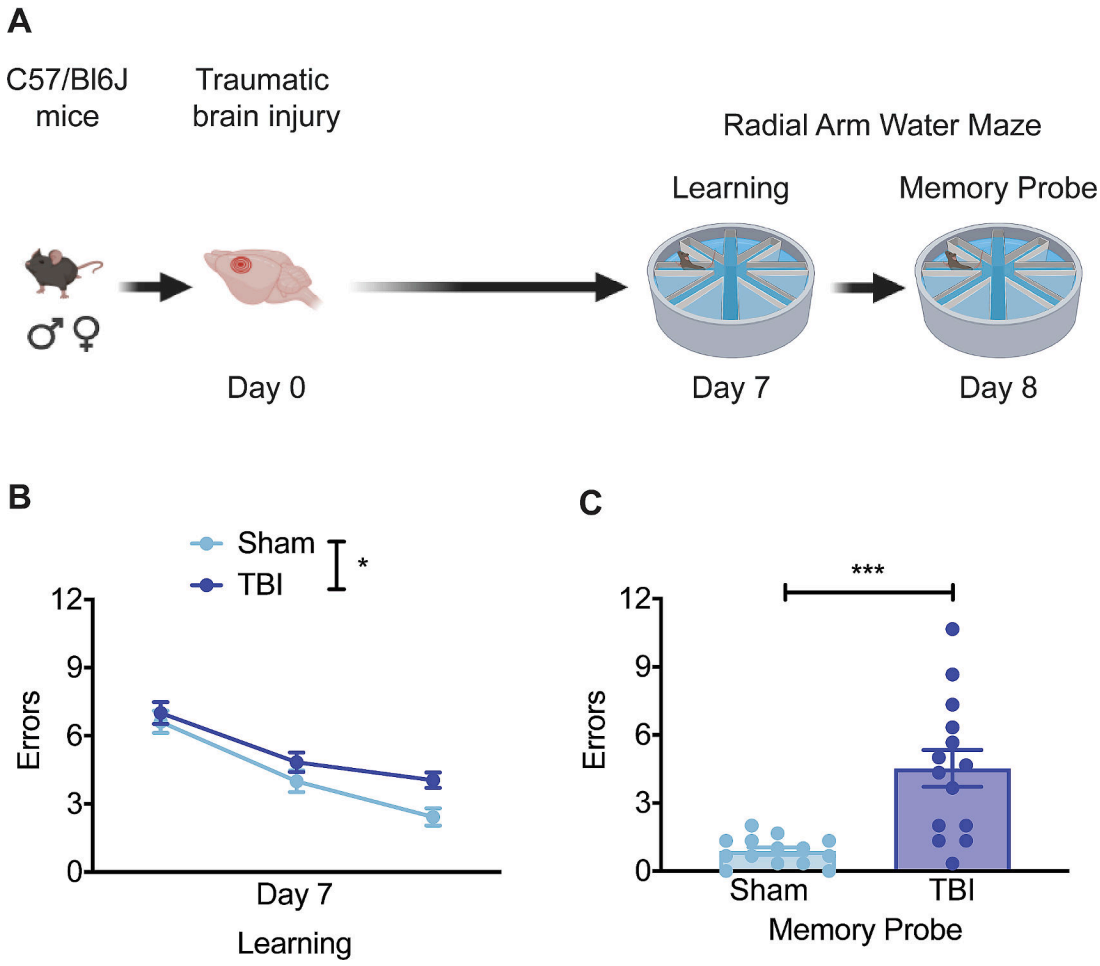

Fig. 1.

Traumatic Brain Injury Induces Spatial Learning and Memory Deficits. (A) Experimental Design- Adult male and female mice were subjected to sham or TBI surgery. Seven days later spatial learning and memory was measured with the radial arm water maze. Animals ran 3 blocks (3 trials/block) during one learning day (day 7) and one block for a memory probe (day 8). (B) The TBI group made significantly more errors over the course of learning when compared with sham mice (significant group differences denoted. Two-way repeated measures ANOVA revealed a significant time ($p = 0.0001$) and injury ($p = 0.01$) effect. Dot depicts group mean and SEM. (C) TBI impaired hippocampal-dependent spatial memory in mice during the memory probe on day 8. Unpaired *t*-test with Welch's correction ($p = 0.0006$). Individual animals plotted, bar depicts group mean and SEM. *$p < 0.05$, ***$p < 0.001$. n : Males Sham = 8; Females Sham = 7; Males TBI = 6; Females TBI = 8.

Author Manuscript Author Manuscript Author Manuscript Author Manuscript

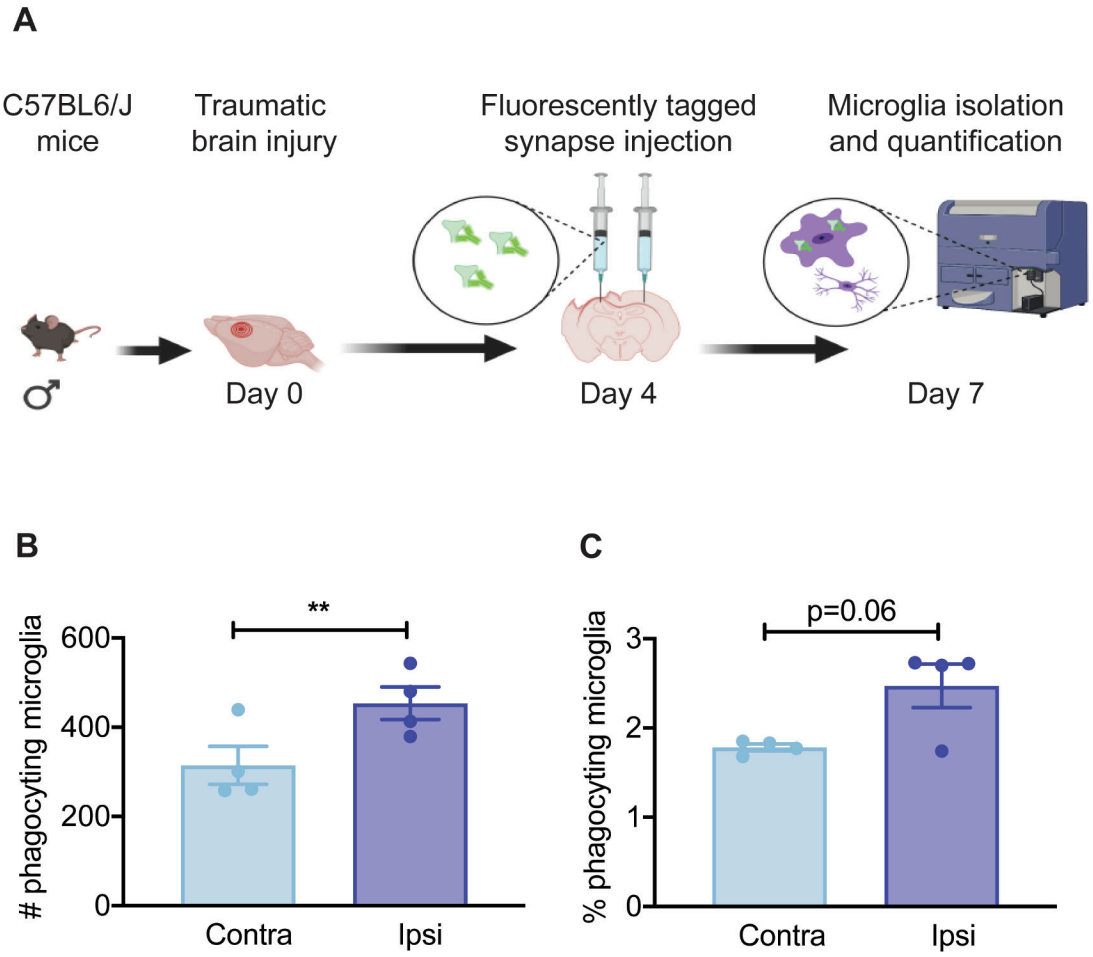

Fig. 2.

Increase in Microglial Phagocytosis of Synapses after Trauma. (A) Experimental design: Male animals received TBI surgery. Four days post injury fluorescent antibody-labeled PSD-95 synapse particles are injected into the ipsilateral (injured) and contralateral (uninjured) hippocampus. On day seven days microglia were isolated and phagocytic activity was quantified by measuring the percentage of microglia that engulf labeled synapses ($CD45^{lo}$, $CD11b^{+}$ co-expressing with intracellular PSD-95-FITC). (B,C) TBI induces synaptosome phagocytosis by microglia in the ipsilateral hemisphere when compared to the contralateral hemisphere. Increases were measured by (B) raw number and (C) percentages. Student *t*-test used to determine differences between groups. Individual animals plotted, bar depicts group mean and SEM. **p $<$0.01. n: Male TBI contralateral hemisphere = 4; Male TBI ipsilateral hemisphere = 4.

Author Manuscript Author Manuscript Author Manuscript Author Manuscript

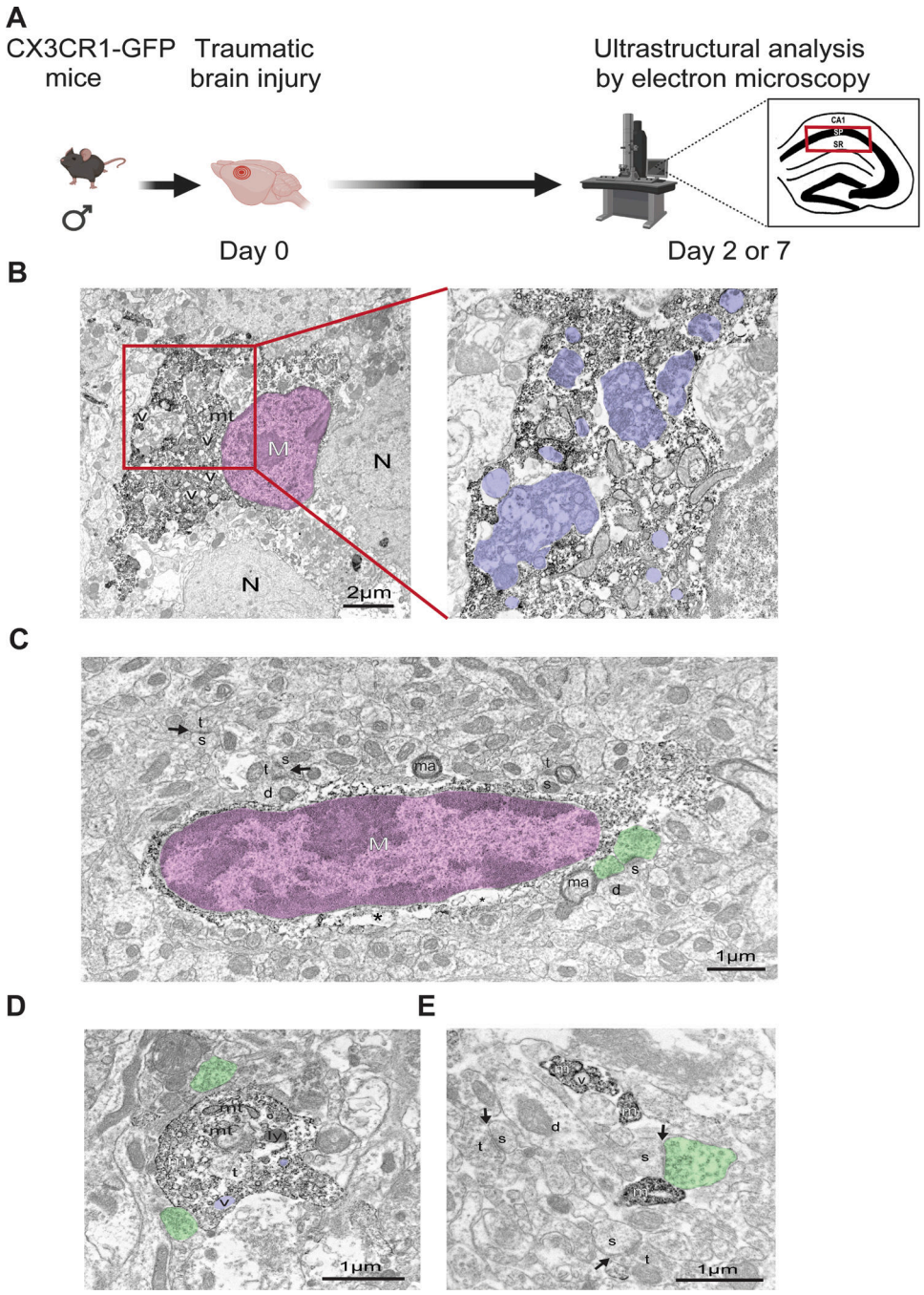

Fig. 3.

Ultrastructural Analysis of Trauma-Induced Microglia Phagocytic Phenotype. (A) Experimental design: CX3CR1GFP/+ (in a C57BL6J background) male mice received unilateral, focal TBI surgery. Two or seven days later brains were extracted for ultrastructural analysis using immunocytochemical transmission electron microscopy (immunoTEM) against GFP, comparing the ipsi (injured)- *versus* contralateral (uninjured) hippocampus. Examination occurred in dorsal hippocampus CA1. (B-E) Electron micrographs showing examples of microglial cell body and processes stained for GFP

Author Manuscript Author Manuscript Author Manuscript Author Manuscript

with peroxidase in the hippocampus CA1 of TBI mice, ipsilateral or contralateral to the lesion. (B) Microglial cell body observed ipsilateral to the lesion, two days after injury, that contains a large number of phagocytic inclusions, in addition to juxtaposing two neuronal cell bodies and several axon terminals. (C) Microglial cell body observed contralateral to the lesion, seven days after the injury, that is devoid of cellular inclusions, but contacting axon terminals and other elements among the neuropil. (D) Microglial process observed ipsilateral to the lesion seven days after injury that contains phagocytic inclusions including one with still intact synaptic vesicles recognized by their 40-nm diameter and distinctive morphology, indicating its axon terminal nature. (E) Microglial processes observed contralateral to the lesion, seven days after injury, that are largely devoid of cellular inclusions, except for a vacuole in a process, yet making extensive contacts with pre- and post-synaptic elements. *EM notations*: microglia-contacted axon terminals = t, pseudocolored in green; dendrite = d; dendritic spine = s; lysosome = ly; microglial cell body = M; nucleus pseudocolored in fuchsia; microglial process = m; mitochondrion = mt; myelinated axon = ma, neuronal cell body = N; phagocytic inclusions = pseudocolored in purple; vacuole = v. Arrows point to synapses.

Author Manuscript Author Manuscript Author Manuscript Author Manuscript

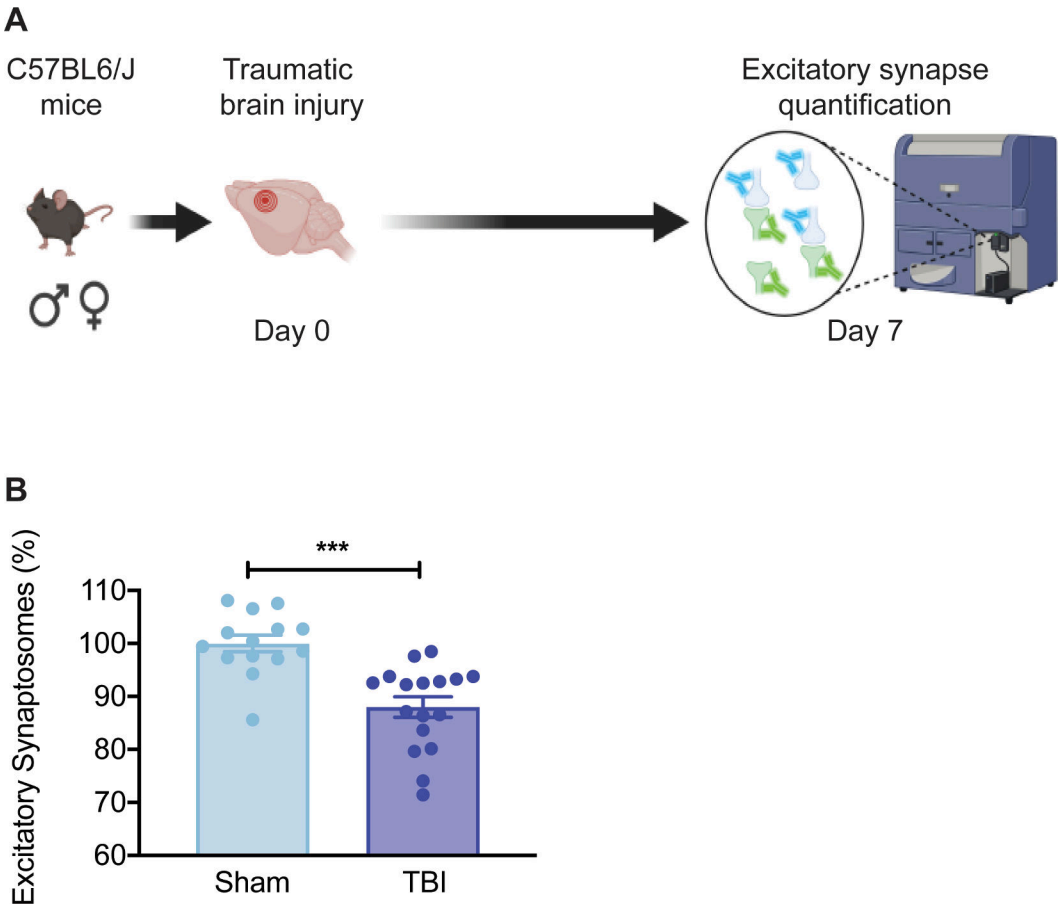

Fig. 4.

Trauma-induces Synapse Loss. (A) Experimental Design- Hippocampi were collected from TBI or sham male and female animals at 7 dpi. The ipsilateral hippocampus was extracted. Synaptosomes were isolated by sucrose gradient followed by size calibration beads, then co-expression of excitatory pre and post synaptic markers- pre-synaptic marker Synapsin-1 and post synaptic marker PSD-95. (B) Significant decreases in total synaptosome numbers in the TBI (7 dpi) group when compared to Sham group. Student *t*-test with Welch correction used to determine differences between groups. Individual animals plotted, bar depicts group mean and SEM. ***p <0.001. n: Male Sham = 5; Female Sham = 9; Male TBI = 8 Female TBI = 9.

Author Manuscript Author Manuscript Author Manuscript Author Manuscript

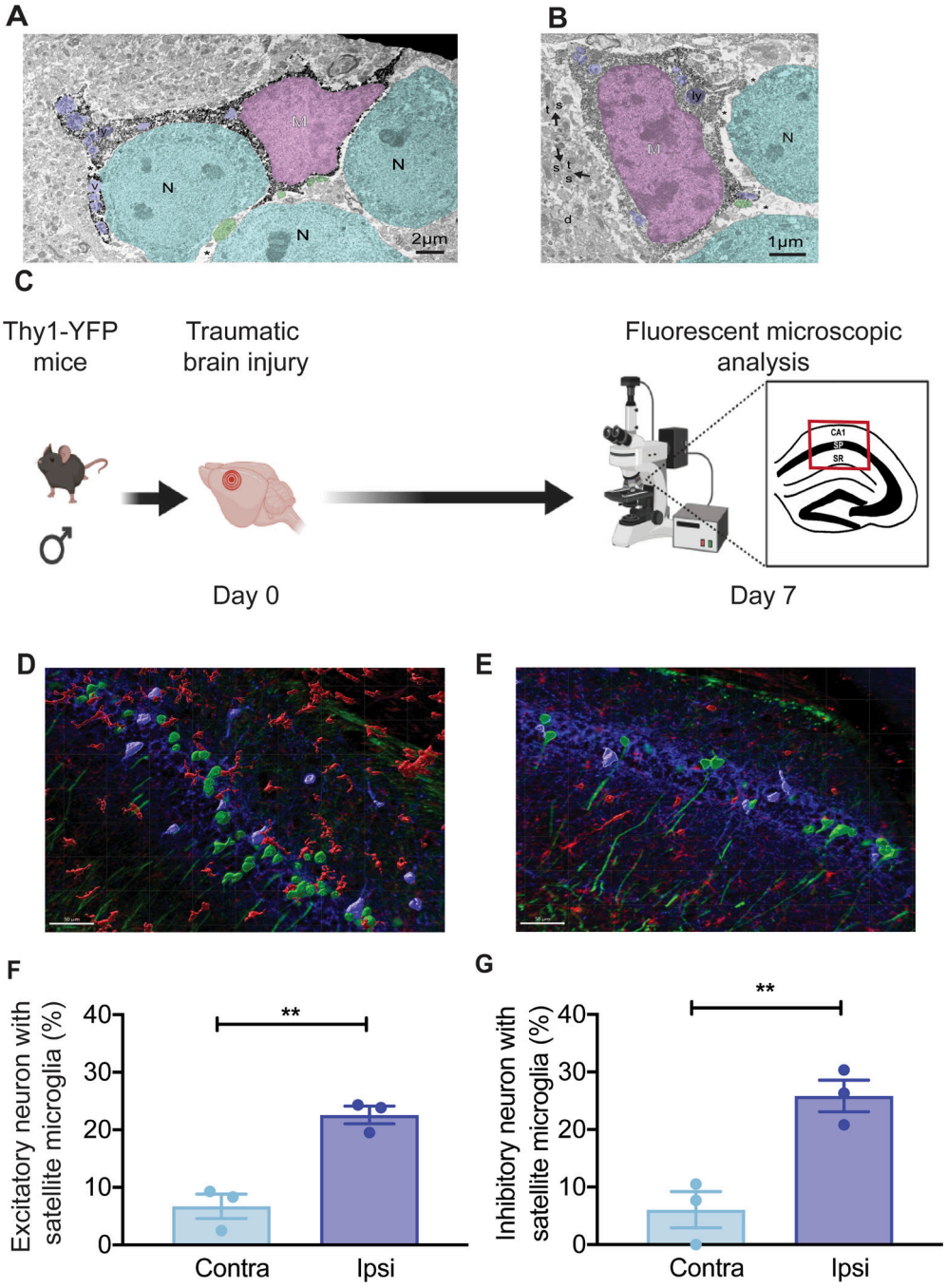

Fig. 5.

Increase in Satellite Microglia Interacting with Excitatory and Inhibitory Neuronal Somata after Trauma. (A,B) Electron micrographs showing examples of microglial cell bodies stained for GFP with peroxidase in dorsal CA1 after TBI, ipsilateral to the lesion: (A) Microglial cell body stained for GFP by peroxidase observed in the pyramidal cell layer ensheaths a neuronal cell body and contacts two additional neurons while containing several phagocytic inclusions including vacuoles and lysosomes. Microglia-associated pockets of extracellular space are shown by asterisks. (B) Microglial cell body observed in dorsal

Author Manuscript Author Manuscript Author Manuscript Author Manuscript

CA1 which also ensheaths a neuronal cell body, contains cellular inclusions and makes contacts with axon terminals in the neuropil. Arrows point to synapses. *EM notations*: Microglia = M, nucleus pseudocolored in fuchsia; Neuronal cell body = N, pseudocolored in cyan; vacuole = v, pseudocolored in purple; lysosome = ly, pseudocolored in purple; * = microglia-associated pocket of extracellular space; microglial contacted axon terminal = pseudocolored in green; arrows = synapse; dendritic spine = s; axon terminal = t, d = dendrite. (C) Experimental Design- Brains were collected from TBI male Thy1-YFP expressing animals at 7 dpi. Brain sections containing the dorsal hippocampus CA1 were stained with IBA1 (denoted in red) to denote microglia. Confocal microscopy followed by Imaris quantification identified the proportion of Thy1-YFP-positive excitatory neurons (denoted in green) with satellite microglia in the ipsi- (D) and contralateral (E) CA1 *stratum pyramidale*. (F) Significant increases in the percentage of excitatory neuron somata with satellite microglia were observed when comparing the ipsi with the contralateral hemisphere. (G) Significant increases in the percentage of PV-positive inhibitory neuron somata (denoted in purple) with adjacent satellite microglia were measured when comparing the ipsi with the contralateral hemisphere. Images were acquired on a Nikon High Speed Widefield Confocal microscope (Ti inverted fluorescence; CSU-W1) at the UCSF Nikon Imaging Center. 200x magnification. Student *t*-test. Individual animals plotted, bar depicts group mean and SEM. **$p < 0.01$. n: Male TBI contralateral = 3; Male TBI ipsilateral = 3.

Author Manuscript Author Manuscript Author Manuscript Author Manuscript

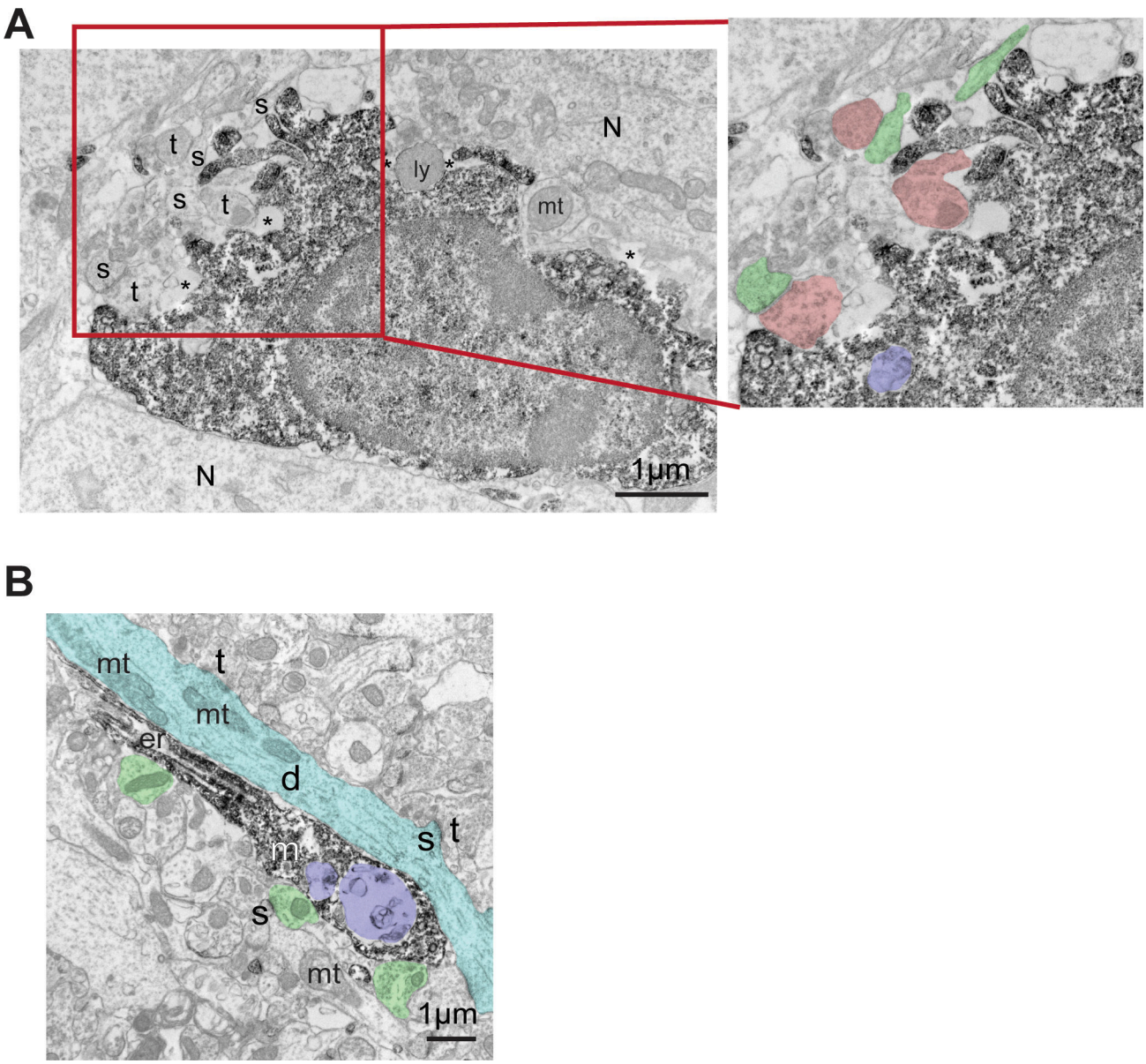

Fig. 6.

Increase in Microglial Dendritic Synaptic Interaction with TBI. (A) Microglial cell body stained for GFP with peroxidase seen extending pseudopodia that contact axon terminals and containing phagocytic inclusions in the pyramidal cell layer of TBI mice, ipsilateral to the lesion, seven days after injury. Microglia-associated pockets of extracellular space are shown by asterisks (B) Example of microglial process stained for GFP with peroxidase in the dorsal hippocampal CA1 of TBI mice, ipsilateral to the lesion, seven days after injury. The process is ensheathing a dendrite, without any axon terminal innervation or astrocytic process in between them and contains phagocytic inclusions contacting axon terminals. *EM notations:* axon terminal = t; pseudocolored in green; dendrite = d; pseudocolored in cyan; dendritic spine = s; pseudocolored in pink; endoplasmic reticulum = er; lysosome = ly; mitochondrion

= mt; neuron = N; microglial process = m; * = microglia-associated pocket of extracellular space; phagocytic inclusion = pseudocolored in purple.

Author Manuscript Author Manuscript Author Manuscript Author Manuscript

Author Manuscript Author Manuscript Author Manuscript Author Manuscript

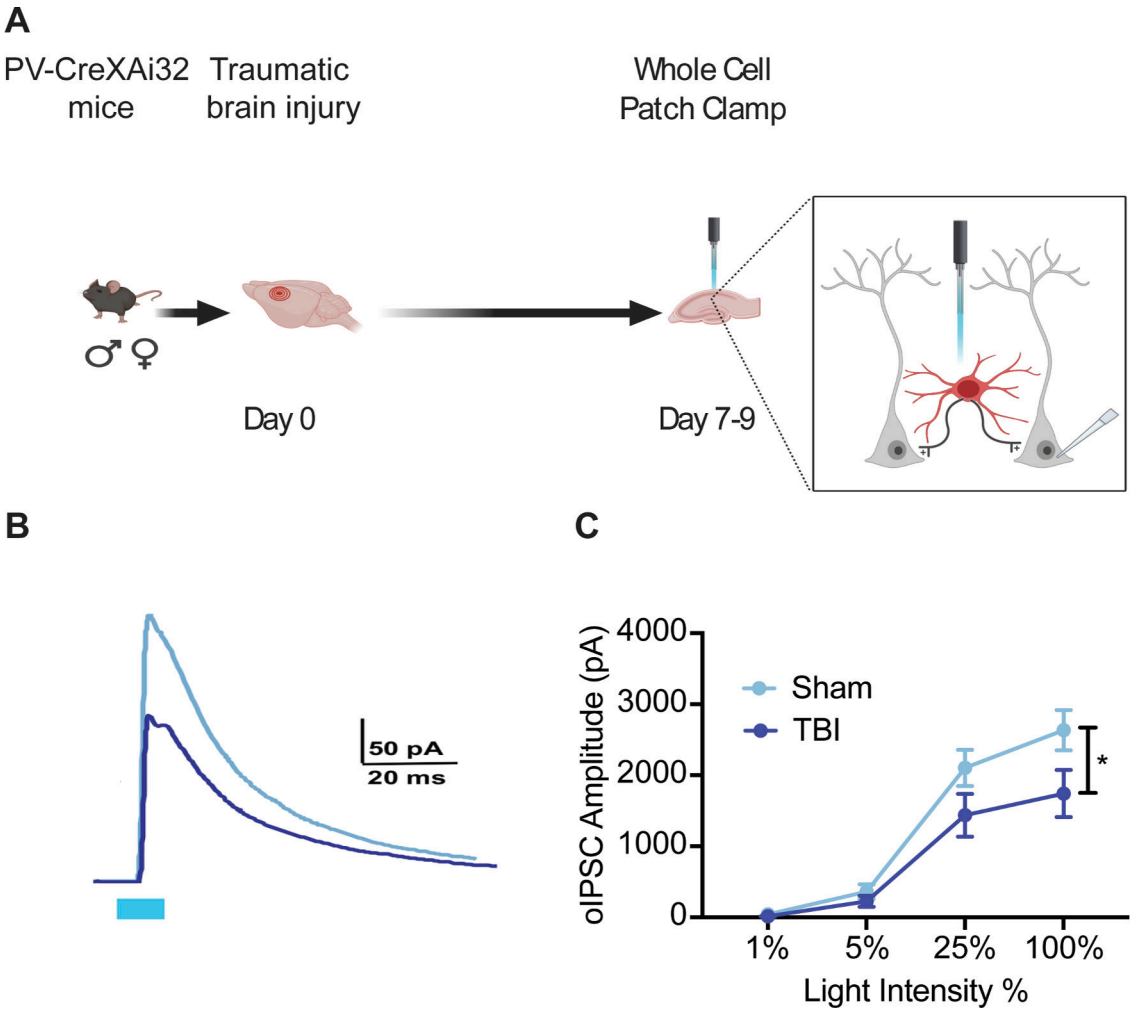

Fig. 7.

Impairment of Inhibitory Synaptic Input after Trauma. (A) Experimental Design- A 10 ms flash of blue light is used to activate ChR2 (a light-sensitive cation channel) expressed exclusively in PV + inhibitory neurons while the corresponding evoked inhibitory synaptic response is recorded in CA1 pyramidal neurons. (B) Example optogenetically-evoked inhibitory post-synaptic current (oIPSC) recorded in TBI (dark blue) and sham (light blue) neurons. (**C**) A reduced amplitude of the oIPSC with higher light intensities is identified when comparing TBI to Sham groups. Two-way repeated measures ANOVA revealed a significant light × TBI interaction ($p = 0.0354$). Bonferroni post-hoc analysis confirmed a significant reduction with TBI at the 100% light intensity ($p = 0.0208$). Circles depict group means and bars indicate SEM. n: TBI neurons = 11 (from 4 mice), Sham neurons = 9 (from 4 mice).

Author Manuscript

Author Manuscript

Author Manuscript

Author Manuscript

Table 1

Quantification of Ultrastructural Analysis by Immunocytochemical Transmission Electron Microscopy on Day 2 post injury. Male C57Bl6J mice received unilateral, focal TBI surgery. Two days post injury brains were extracted for ultrastructural analysis by immunocytochemical transmission electron microscopy against GFP, comparing the ipsi (injured)- *versus* contralateral (uninjured) hippocampus. Examination and quantification occurred in dorsal hippocampus CA1.

DAY 2	Contra	Ipsi	p value
Cellular Inclusions	2.0 ± 0.5	5.3 ± 1.2	0.02 *
Synaptic contacts	1.0 ± 0.3	1.3 ± 0.2	0.28
Myelinated axon contacts	0.0 ± 0.0	0.1 ± 0.1	0.10
Digested vacuoles	0.7 ± 0.2	2.8 ± 1.0	0.20
Extracellular debris	0.7 ± 0.1	0.7 ± 0.1	0.99
Lipid bodies	0.2 ± 0.1	0.0 ± 0.0	0.53
Lipofuscin granules	0.1 ± 0.1	0.0 ± 0.0	0.99
ER/Golgi Dilation	0.1 ± 0.0	0.3 ± 0.1	0.4

Values are expressed as average number per microglial cell body profile (mean +/− SEM). Mann-Whitney test was used to determine differences between groups.

* $p < 0.05$.

n: Contralateral cells = 17, Ipsilateral cells = 16.

Author Manuscript

Author Manuscript

Author Manuscript

Author Manuscript

Table 2

Quantification of Ultrastructural Analysis by Immunocytochemical Transmission Electron Microscopy on Day 7 post injury. Male C57Bl6J mice received unilateral, focal TBI surgery. Seven days post injury brains were extracted for ultrastructural analysis by immunocytochemical transmission electron microscopy against GFP, comparing the ipsi (injured)- *versus* contralateral (uninjured) hippocampus. Examination and quantification occurred in dorsal hippocampus CA1.

DAY 7	Contra	Ipsi	p value
Digested Vacuoles	0.0 ± 0.0	0.3 ± 0.1	0.018 *
Synaptic contacts	0.1 ± 0.0	0.8 ± 0.2	0.012 *
Myelinated axon contacts	0.1 ± 0.0	0.3 ± 0.1	0.18
Cellular Inclusions	1.4 ± 0.3	3.0 ± 0.9	0.20
Extracellular debris	0.7 ± 0.1	0.8 ± 0.0	0.65
Lipid bodies	0.0 ± 0.0	0.1 ± 0.0	0.60
Lipofuscin granules	0.0 ± 0.0	0.0 ± 0.0	0.99
ER/Golgi Dilation	0.0 ± 0.0	0.3 ± 0.1	0.018 *

Values are expressed as average number per microglial cell body profile (mean +/− SEM). Mann-Whitney test was used to determine differences between groups.

* $p < 0.05$

** $p < 0.01$.

n: Contralateral cells = 17, Ipsilateral cells = 16.